Scripta Materialia 204 (2021) 114161

Contents lists available at ScienceDirect

Scripta Materialia

journal homepage: www.elsevier.com/locate/scriptamat

Friction stir welding of γ-fcc dominated metastable high entropy alloy: Microstructural evolution and strength

Sanya Gupta[a], Priyanka Agrawal[a,b], Saurabh S. Nene[a,c], Rajiv S. Mishra[a,b,*]

[a] Center for Friction Stir Processing, Department of Materials Science and Engineering, University of North Texas, Denton, TX 76207, USA
[b] Advanced Materials and Manufacturing Processes Institute, University of North Texas, Denton, TX 76207, USA
[c] Indian Institute of Technology, Jodhpur, Rajasthan, India

ARTICLE INFO

Article history:
Received 13 April 2021
Revised 3 July 2021
Accepted 19 July 2021
Available online 28 July 2021

Keywords:
Friction stir welding
Differential scanning calorimetry
Metastable high entropy alloys
Tensile properties
Hardness

ABSTRACT

A systematic study of butt friction stir welding of a recently developed Cu-containing metastable high entropy alloy (HEA) was conducted. Different zones of the weld were evaluated using mechanical testing, microstructural characterization, and differential scanning calorimetry (DSC). The nugget exhibited high tensile strength as a result of the refined equiaxed microstructure. Interestingly, the heat affected zone, which is known to be the weakest region, exhibited an excellent combination of strength and ductility as compared to the base metal. DSC was explored as a novel and quick technique to obtain enthalpy information and thus understand the TRIP effect.

High entropy alloys are promising structural materials with equiatomic or non-equiatomic compositions because of good combination of strength and ductility [1–3]. Further improvement in mechanical properties was reported by Li et al. [4] with the introduction of dual-phase HEA (DP-HEA). Since around 2010, HEAs have been studied widely for multifaceted properties such as strength and ductility [5,6], irradiation resistance [7], corrosion resistance [8], and high fracture toughness [9,10]. Apart from the listed properties, weldability, which is a fundamental property determining the usability of a structural material has started getting attention [11–13]. HEAs are designed with the aim to obtain low stacking fault energy (SFE), thus aiding the transformation or twin-induced plasticity (TRIP or TWIP effect) that leads to improved work hardening and thus strength of the material. Recently, Nene et al. [14,15] reported the addition of Si to DP-HEA, thus introducing a new alloy composition, $Fe_{40}Mn_{20}Co_{20}Cr_{15}Si_5$ (CS-HEA), with reduced SFE of ~6.31 mJ/m^2 as reported by Frank et al. [16] via neutron diffraction.

A recent study confirmed that Cu added to CS-HEA, with the help of a novel high-throughput technique - friction stir gradient alloying (FSGA) [17,18], enhanced microstructural evolution and furthered the study of its mechanical properties. The addition of Cu resulted in the stabilization of γ (f.c.c) microstructure along with concurrent grain refinement. Furthermore, Cu addition led to a decrease in metastability and delayed the onset of TRIP effect, thus improved overall work hardening [8,17]. Friction stir processed (FSP) Cu-stabilized CS-HEA ($Fe_{38.5}Mn_{20}Co_{20}Cr_{15}Si_5Cu_{1.5}$, henceforth referred to as Cu-HEA) tested for corrosion resistance [8], and cyclic behavior [19], proved to have superior properties.

Various FSP studies have been based on the principle of friction stir welding (FSW) as a tool for microstructural modification [20–22]. FSW is a promising solid-state joining technique that introduces excellent properties like high ultimate tensile strength (UTS) and joint efficiency. High strength is due to the synergistic action of heat as well as plastic deformation on materials and thus leading to the formation of fine grain size in the nugget (stirred zone) and phase evolution during tensile deformation [23,24]. A study comparing FSW and laser welding (LW) for high entropy alloy CrMnFeCoNi showed grain size refinement by a factor of ~14% compared to the base material (BM) with superior weldability and strength; whereas LW reported fluctuations in the fusion zone [25].

In the present work, the weldability of metastable Cu-HEA γ (f.c.c) dominated alloy is explored using FSW. A detailed study with respect to strength based on phase transformation in each of the weld zones: nugget, heat affected zone (HAZ), and base material (BM) was carried out via mechanical testing, microstructural characterization, and differential scanning calorimetry (DSC).

$Fe_{38.5}Mn_{20}Co_{20}Cr_{15}Si_5Cu_{1.5}$ HEA (Cu-HEA) was prepared by casting in a vacuum induction melting furnace and subsequent rolling. The rolled sheet was homogenized at 900°C for 8 hrs followed by water quenching. For FSW, two rectangular pieces of

* Corresponding author.
E-mail address: Rajiv.Mishra@unt.edu (R.S. Mishra).

https://doi.org/10.1016/j.scriptamat.2021.114161
1359-6462/

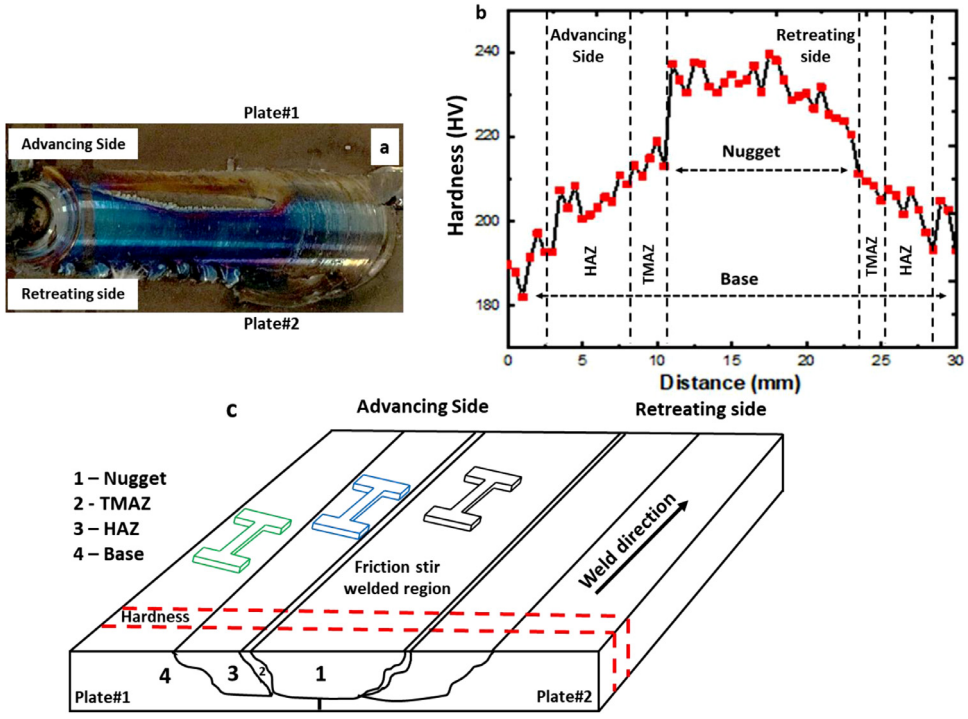

Fig. 1. (a) Macro-image of welded block via friction stir welding (FSW), (b) hardness profile across the cross-section of FSW run, and (c) schematic of the FSW and locations marked for the tensile samples machined out.

(160 × 75 × 6) mm^3 were cut using electric machine discharge (EDM) from the rolled plate. FSW was carried out in the air on an MTI RM-1 friction stir welding machine with tool rotation rate of 350 revolutions per minute (RPM), welding speed of 50.8 mm/min, plunge depth of 4.4 mm, and tilt angle of -2.5^0. A W-Re tool was used with 16 mm shoulder diameter, 7.5 mm root diameter, and pin diameter and length of 5 mm and 4 mm, respectively. A Cu backing plate was used for higher heat dissipation. Fig. 1(a) shows the macro-image of the butt friction stir welded plates. The cross-section of the weld was cut using EDM and subsequent grinding and polishing were carried out for hardness testing and microstructural characterization. The specimen was prepared to start from 600-grade emery paper polishing followed by final polishing with 0.02 µm colloidal silica to obtain the surface with a mirror finish. Vickers microhardness along the centerline on the cross-section was measured in intervals of 0.5 mm with a load of 0.5 kg and dwell time of 10 seconds. Results from the hardness test of the weld cross-section (Fig. 1(b)) helped to identify all the zones observed after FSW (Fig. 1(c)). The microstructural studies for each zone were carried out using the FEI NOVA Nano scanning electron microscope (SEM) with electron backscattered diffraction (EBSD) measurements obtained using a Hikari Super EBSD camera. The EBSD data were analyzed using TSL OIM 8 software to get an estimate of grain size and phase fraction of different zones in the microstructure. Microstructural characterization was followed by tensile tests for the identified zones. For the tensile testing, rectangular 1 mm-thick dog bone-shaped mini-tensile specimens were carefully machined using a computer numerical control (CNC) machine from 1 mm below the surface within the nugget, HAZ, and BM as shown in Fig. 1(b). Gauge length and width of the tensile specimens were ~5 mm and ~1.25 mm, respectively. The samples were tested at room temperature with an initial strain rate of 10^{-3} s^{-1}. The width identified for thermo-mechanically affected zone (TMAZ) was not big enough to mill a tensile sample. Differential scanning calorimetry (DSC) is traditionally used and reported to measure the melting point, nucleation of new phases, and allotropic transformation. In the current study, ***DSC was used as a novel approach to understand the metastability of the TRIP HEA*** by carrying out experiments before and after the deformation. For the DSC study, samples were extracted from the tensile tested samples for undeformed (from the grip) and deformed regions (from the gauge fractured region) for all three zones. A Netzsch 204F1 Phoenix® system was used to perform and analyze the data with a heating rate of 20°C/minute. Fig. 1(b) gives hardness values across the weld cross-section. Hardness values for the nugget region and HAZ were much higher than for the BM, with not much difference between the advancing and retreating sides. The average hardness values for the nugget, HAZ and BM were ~235 HV, ~205 HV, and ~195 HV, respectively. The nugget displayed higher hardness due to the combination of dynamic recrystallization and work hardening as reported by Nene et al. [8] and explained by micrographs in subsequent sections. However, the improved HAZ properties are due only to microstructural evolution owing to the thermal effect it experienced during FSW.

Fig. 2(a) captures the phase maps via EBSD measurements of the overall FSW region along with demarcation for all zones, nugget, TMAZ, HAZ, and BM. Fig. 2(b) shows a change in grain size in the nugget as compared to BM as well as the change in phase fraction. The BM depicts grain size more than 50 μm with phase distribution of γ (f.c.c) 79% and ε (h.c.p) 21%. Grain refinement (grain size less than 15 μm) in the nugget region (Fig. 2(b)) is attributed solely to friction stirring that leads to high temperatures and severe deformation in the stirred zone [26]. The nugget also displayed a change in phase fraction where γ (f.c.c) is 92% and ε (h.c.p) is 8%, making γ (f.c.c) more stable (Fig. 2(b)). The increased percentage of γ (f.c.c) in the nugget compared to BM is attributed to temperature and strain [4,18–20]. Higher γ (f.c.c) in nugget can also be attributed to the dissolution of Cu in solid solution, which is observed in the EDS maps as shown in Fig. 2(c_1–c_3). The base material had regions of higher and lower Cu concentration. In the nugget, the value of Cu in the analyzed region is close to the nominal value of 1.5%.

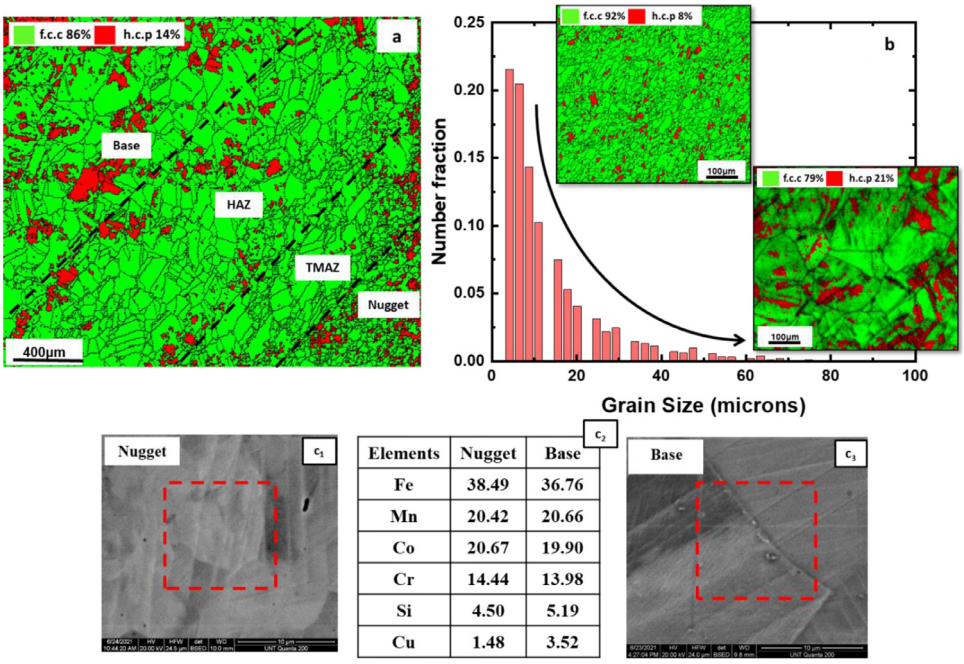

Elements	Nugget	Base
Fe	38.49	36.76
Mn	20.42	20.66
Co	20.67	19.90
Cr	14.44	13.98
Si	4.50	5.19
Cu	1.48	3.52

Fig. 2. EBSD results for overall FSW region. (a) Phase maps where green color is for γ (f.c.c) phase and red is for ε (h.c.p) phase, (b) a plot representing the grain size distribution across the weld along with the phase maps for nugget and BM, and (c_1-c_3) represents the EDS results for nugget and BM.

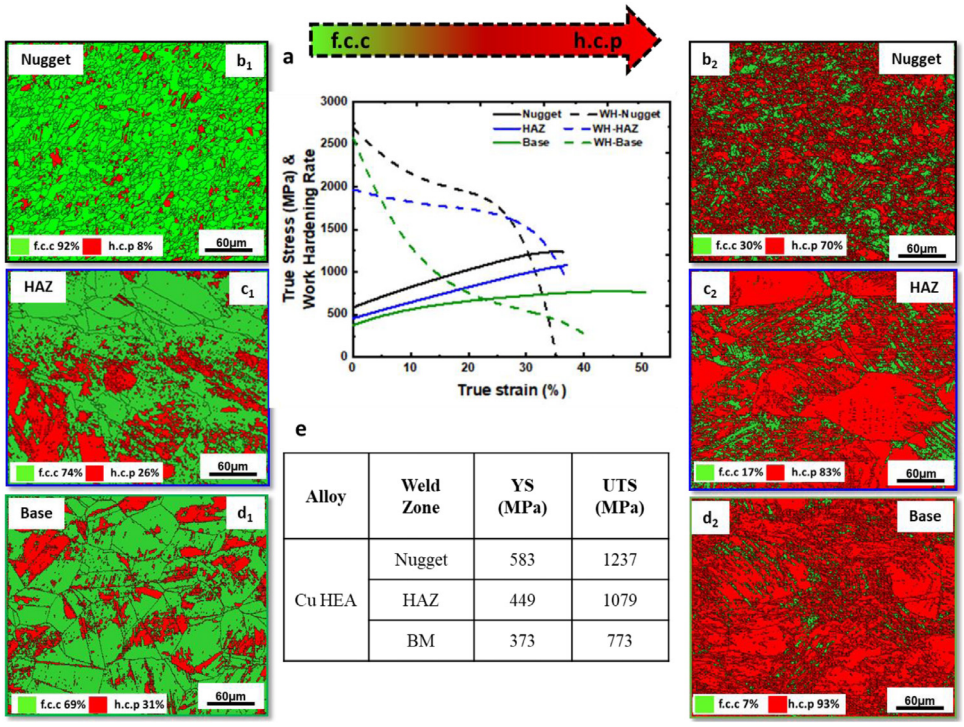

e

Alloy	Weld Zone	YS (MPa)	UTS (MPa)
Cu HEA	Nugget	583	1237
	HAZ	449	1079
	BM	373	773

Fig. 3. (a) True stress-strain curves along with work hardening rates for all the regions; (b_1, c_1, and d_1) are the phase maps for the nugget, HAZ and BM, respectively, before the deformation; and (b_2, c_2, and d_2) are the phase maps for the nugget, HAZ and BM, respectively, after deformation; and (e) tabulated tensile properties for different weld zones.

True stress-strain and work hardenability (WH) curves of all three zones are presented in Fig. 3(a). This comparison allows discussion of two key aspects. First, does initial phase content have significant effect on subsequent phase transformation? Second, does the grain refinement impact the overall transformation? Compared to the BM, the curves for the nugget (finer grain size and higher starting γ (f.c.c) phase fraction) and the HAZ (higher starting γ (f.c.c) phase fraction than the BM but with pockets of fine grains) displayed higher YS and UTS. Note that while the YS depends only on the starting microstructure, the reason for the higher UTS in the nugget and specifically in the HAZ can be explained with the help of WH curves [27–29]. The increase in the YS, therefore, can be attributed to the finer overall grain size in the nugget and pocket of finer grains in the HAZ. The hump in the WH curves in Fig. 3(a) corresponds to the TWIP/TRIP effect, which shifts to higher stresses and lower strain levels as one trav-

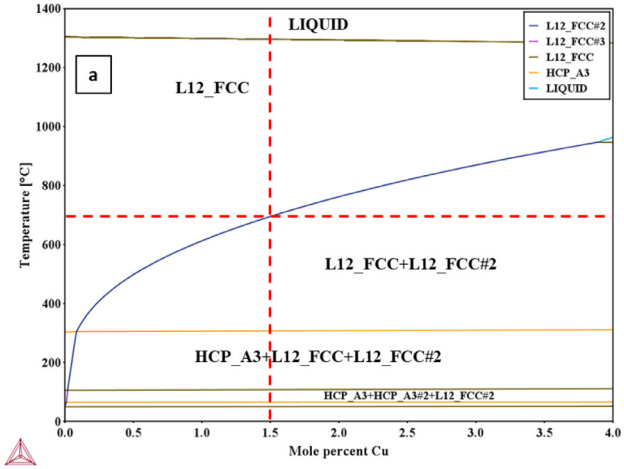

b

Phase/ Zones	Undeformed Region		Deformed Region	
	fcc	hcp	fcc	hcp
Nugget	92%	8%	30%	70%
HAZ	74%	26%	17%	83%
Base	69%	31%	7%	93%

e

Phase/ Zones	Undeformed Region (ΔH=kJ/mol)	Deformed Region (ΔH=kJ/mol)
Nugget	1208	664
HAZ	1236	789
Base	1274	980

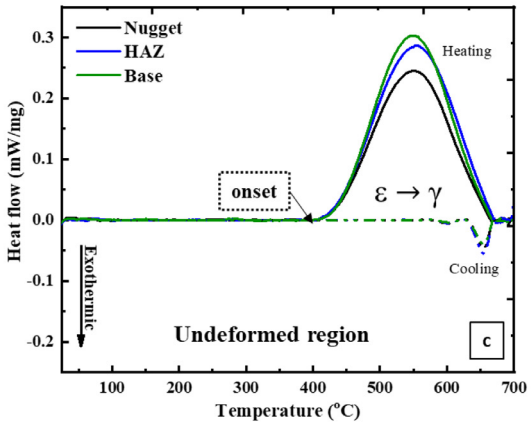

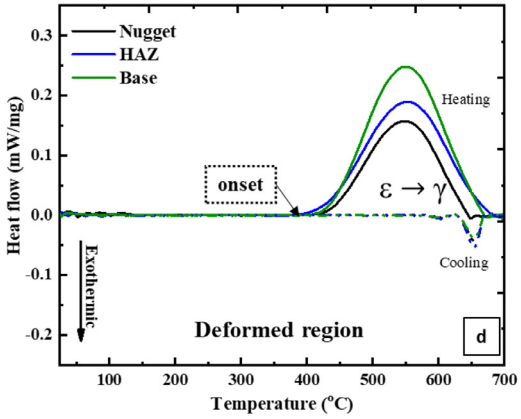

Fig. 4. DSC study to quantify the energy change associated with deformation. (a) Cu-HEA phase diagram with TCFE9 database, (b) summary of the changes in microstructural phase fraction for undeformed and deformed regions for weld regions, (c) DSC curves for nugget, HAZ and BM for the undeformed region, and (d) DSC curves for nugget, HAZ, and BM for the deformed region, and (e) summary of experimental enthalpy calculated for undeformed and deformed regions.

els from BM to HAZ to nugget [12,30]. Tian et al. [31] reported that the TWIP/TRIP is very sensitive to grain size where the onset shifts to lower strain with a decrease in grain size. In this study, as can be noted from Fig. 3, the change or increase in transformed ε (h.c.p) % was quite similar for all the three zones (% transformation is 62% for nugget, 57% for HAZ and 62% for the BM). It is important to split the overall response into the onset of transformation and total extent of transformation. These two aspects impact the overall stress-strain curve in different ways. So, while the onset of TRIP/TWIP effect in nugget can be argued based on the grain size effect (comparison of Fig. 3(a) with (b_1) and (b_2)), the higher fraction of γ (f.c.c) phase fraction does not add additional uniform ductility as the extent of deformation induced transformation is same as the base material. Comparison of HAZ and BM provides insight on the effect of starting phase fraction with relatively similar grain size. The deformed phase map of BM (Fig. 3(d_2)) shows a higher activity of slip (or more slip lines) as compared to HAZ (Fig. 3(c_2)), leading to more transformed ε (h.c.p) % in BM. A study carried out by Sinha et al. [32] on the same alloy shows reversal of ε (h.c.p) to γ (f.c.c) on annealing (heating). The phase reversal leads to finer grains. Fig. 3(c2) does show that the retained or non-transformed pockets of γ (f.c.c) phase are very fine. Fig. 3(e) summarizes the tensile properties for these three regions. The results from microscopy and mechanical testing show that FSW causes Cu-HEA to exhibit microstructural phase evolution and exhibited a unique variation in grain size that led to a significant increase in strength. This is very encouraging as the entire joint shows properties higher than the BM.

Further, DSC was carried out in an attempt to understand the metastability of HEAs instead of going through rigorous experiments to calculate the change in enthalpy, ΔH, required to obtain $\Delta G^{\gamma\to\varepsilon}$. Fig. 4 represents the DSC study of samples in undeformed and deformed conditions to understand the phase transformation. The samples were heated to 700°C to cover the transformation temperature with a heating rate of 20°C/min and cooled to room temperature. An endothermic reaction is depicted as a hill (upward curve), while the exothermic reaction is drawn as a valley (downward curve). The endothermic reactions are related to phase transformation, i.e. ε (h.c.p) to γ (f.c.c). The area under the peaks corresponds to the change in enthalpy, ΔH. Table in Fig. 4(b) presents the change in the microstructural phase fraction for undeformed and deformed regions for nugget, HAZ, and BM (from Fig. 3). The DSC for undeformed and deformed regions are captured in Fig. 4(c) and (d), respectively. The solid line in the curve represents the heating and the dotted line as cooling curves. The onset for the endothermic reactions in the heating curve is ~ 400°C which signifies the phase transformation, i.e. ε (h.c.p) is transforming to γ (f.c.c) for all the regions, as noted from Fig. 4(a). For undeformed samples in Fig. 4(c), the highest peak is for BM and the lowest for nugget. These results when compared with tabulated phase fractions in Fig. 4(b), show that the condition with more ε (h.c.p) leads to higher peak, indicating more energy associated with transformation to γ (f.c.c). Fig. 4(e) lists the experimental change in enthalpy calculations for all zones undeformed (calculated change in enthalpy for nugget ~ 1208 kJ/mol, HAZ ~ 1236 kJ/mol and BM ~1274 kJ/mol) and deformed regions (calculated change in enthalpy for nugget ~664 kJ/mol, HAZ ~789 kJ/mol and BM ~980 kJ/mol), ob-

tained by the area under the curve, representing different enthalpy states [33,34]. Two trends can be captured from these results. In undeformed specimens, the energy associated with phase transformation is dependent on grain size as well as the retained ε (h.c.p) phase. On comparing undeformed and deformed samples (Fig. 4(c) and (d)), the peaks for the specimens from deformed region are shorter, hinting at lower energy required for transformation. The reason for the energy difference for the undeformed region and the deformed can be explained by $\Delta G^{\gamma\rightarrow\varepsilon}$ for $\gamma \rightarrow \varepsilon$ transformation [33,34]. The $\Delta G^{\gamma\rightarrow\varepsilon}$ has the entropy ($\Delta S^{\gamma\rightarrow\varepsilon}$) and enthalpy ($\Delta H^{\gamma\rightarrow\varepsilon}$) components. The entropy component can be assumed to be a constant for a given solid solution and the deformation induced $\gamma \rightarrow \varepsilon$ transformation is compositionally invarient. However, the enthalpy of the material is microstructure dependent and changes with the density of microstructural features such as interfaces, dislocations, etc. Mishra et al. [33,34] have postulated that this leads to high enthalpy states in the metastable HEAs which will alter the external stress required for $\gamma \rightarrow \varepsilon$ transformation as well as the reverse transformation. For the deformed region, the elevated enthalpy state makes the transformation from ε (h.c.p) easier in comparison to the undeformed region.

Cu-HEA with the dominant γ (f.c.c) phase was studied for weldability via friction stir welding. The alloy exhibited good combination mechanical properties for all the zones, including enhanced properties of the weld region - nugget (i.e., weld region) and the HAZ. DSC has been introduced as a novel and hands-on technique to study the metastability and the TRIP/TWIP effect in HEAs along with the usual transformation temperature quantitatively.

Declaration of Competing Interest

The authors declare that they have no known competing financial interests or personal relationships that could have appeared to influence the work reported in this paper.

Acknowledgment

The work was carried out under the cooperative agreement of the University of North Texas with the U.S. Army Research Laboratory (W911NF-18-2-0067). The authors thank Materials Research Facility (MRF) at the University of North Texas for access to microscopy facilities.

References

[1] D.B. Miracle, O.N. Senkov, Acta Mater. 122 (2017) 448–511.
[2] B. Cantor, Entropy 16 (2014) 4749–4768.
[3] R.S. Mishra, S.S. Nene, M. Frank, S. Sinha, K. Liu, S. Shukla, J. Alloys Compd. 842 (2020) 155625.
[4] Z. Li, C.C. Tasan, K.G. Pradeep, D. Raabe, Acta Mater. 131 (2017) 323–335.
[5] C. Lee, G. Song, M.C. Gao, R. Feng, P. Chen, J. Brechtl, Y. Chen, K. An, W. Guo, J.D. Poplawsky, S. Li, A.T. Samaei, W. Chen, A. Hu, H. Choo, P.K. Liaw, Acta Mater. 160 (2018) 158–172.
[6] B. Cai, B. Liu, S. Kabra, Y. Wang, K. Yan, P.D. Lee, Y. Liu, Acta Mater. 127 (2017) 471–480.
[7] N.A.P.K. Kumar, C. Li, K.J. Leonard, H. Bei, S.J. Zinkle, Acta Mater. 113 (2016) 230–244.
[8] S.S. Nene, M. Frank, K. Liu, S. Sinha, R.S. Mishra, B.A. McWilliams, K.C. Cho, Scr. Mater. 166 (2019) 168–172.
[9] J.T. Fan, L.J. Zhang, P.F. Yu, M.D. Zhang, D.J. Liu, Z. Zhou, P. Cui, M.Z. Ma, Q. Jing, G. Li, R.P. Liu, Mater. Sci. Eng. A 728 (2018) 30–39.
[10] F. Otto, A. Dlouhý, C. Somsen, H. Bei, G. Eggeler, E.P. George, Acta Mater. 61 (2013) 5743–5755.
[11] E.I. Galindo-Nava, P.E.J. Rivera-Díaz-del-Castillo, Acta Mater. 128 (2017) 120–134.
[12] S. Martin, S. Wolf, U. Martin, L. Krüger, D. Rafaja, Metall. Mater. Trans. A Phys. Metall. Mater. Sci. 47 (2016) 49–58.
[13] S. Sinha, S.S. Nene, M. Frank, K. Liu, P. Agrawal, R.S. Mishra, Sci. Rep. 9 (2019) 13185.
[14] S.S. Nene, M. Frank, K. Liu, S. Sinha, R.S. Mishra, B. McWilliams, K.C. Cho, Scr. Mater. 154 (2018) 163–167.
[15] S.S. Nene, M. Frank, P. Agrawal, S. Sinha, K. Liu, S. Shukla, R.S. Mishra, B.A. McWilliams, K.C. Cho, Mater. Des. 194 (2020) 108968.
[16] M. Frank, Y. Chen, S.S. Nene, S. Sinha, K. Liu, K. An, R.S. Mishra, Mater. Today Commun. 23 (2020) 100858.
[17] S. Shukla, T. Wang, M. Frank, P. Agrawal, S. Sinha, R.A. Mirshams, R.S. Mishra, Mater. Today Commun. 23 (2020) 100869.
[18] P. Agrawal, S. Shukla, S. Gupta, P. Agrawal, R.S. Mishra, Appl. Mater. Today 21 (2020) 100853.
[19] K. Liu, S.S. Nene, M. Frank, S. Sinha, R.S. Mishra, Appl. Mater. Today 15 (2019) 525–530.
[20] M. Komarasamy, T. Wang, K. Liu, L. Reza-Nieto, R.S. Mishra, Scr. Mater. 162 (2018) 38–43.
[21] R.S. Mishra, Z.Y. Ma, Mater. Sci. Eng. R Reports 50 (2005) 1–78.
[22] R.S. Mishra. P.S. De, N. Kumar, in: Friction Stir Welding and Processing: Science and Engineering, Springer, August 2014, p. 338. ISBN-13: 978-3-319-07043-8pages.
[23] W.H. Liu, Y. Wu, J.Y. He, T.G. Nieh, Z.P. Lu, Scr. Mater. 68 (2013) 526–529.
[24] R.S. Mishra, M.W. Mahoney, Mater. Sci. Forum, Trans Tech Publications Ltd 357–359 (2001) 507–514.
[25] M.G. Jo, H.J. Kim, M. Kang, P.P. Madakashira, E.S. Park, J.Y. Suh, D.I. Kim, S.T. Hong, H.N. Han, Met. Mater. Int. 24 (2018) 73–83.
[26] M. Komarasamy, R.S. Mishra, S. Mukherjee, M.L. Young, JOM 67 (2015) 2820–2827.
[27] M. Wang, Z. Li, D. Raabe, Acta Mater. 147 (2018) 236–246.
[28] S.S. Nene, K. Liu, M. Frank, R.S. Mishra, R.E. Brennan, K.C. Cho, Z. Li, D. Raabe, Sci. Rep. 7 (2017) 1–7.
[29] S.S. Nene, M. Frank, K. Liu, R.S. Mishra, B.A. McWilliams, K.C. Cho, Sci. Rep. 8 (2018) 1–8.
[30] W.S. Choi, H.S. Oh, M. Lai, N.V. Malyar, C. Kirchlechner, E.S. Park, P.P. Choi, Scr. Mater. 176 (2020) 122–125.
[31] Y.Z. Tian, L.J. Zhao, S. Chen, A. Shibata, Z.F. Zhang, N. Tsuji, Sci. Rep. 5 (2015) 1–9.
[32] S. Sinha, S.S. Nene, M. Frank, K. Liu, R.S. Mishra, B.A. McWilliams, K.C. Cho, Materialia 6 (2019) 100310.
[33] R.S. Mishra, S.S. Nene, Metall. Mater. Trans. A 52 (2021) 889–896.
[34] R.S. Mishra, R.S. Haridas, P. Agrawal, Mater. Sci. Eng. A 812 (2021) 141085.